Numerical investigation of interface region flows in mass spectrometers: ion transport

Manish Jugroot[1]**, Clinton P T Groth**[1]**, Bruce A Thomson**[2]**,
Vladimir Baranov**[2] **and Bruce A Collings**[2]

[1] Institute for Aerospace Studies, University of Toronto, 4925 Dufferin Street, Toronto,
Ontario, M3H 5T6, Canada
[2] MDS SCIEX, 71 Four Valley Drive, Concord, Ontario, L4K 4V8, Canada

E-mail: groth@utias.utoronto.ca

Abstract
The transport of free ions through highly under-expanded jet flows of neutral
gases and in the presence of applied electric fields is investigated by
continuum-based numerical simulations. In particular, numerical results are
described that are relevant to ion flows occurring in the interface region of
mass spectrometer systems. A five-moment mathematical model and
parallel multi-block numerical solution procedure are developed for
predicting the ion transport. The model incorporates the effects of
ion–neutral collision processes and is used in conjunction with a
Navier–Stokes model and flow solver for the neutral gas to examine the key
features of the ion motion. The influences of the neutral gas flow, electric
field, and flow field geometry on ion mobility are all carefully assessed.
Several ions of varying mass and charge are considered, and the relative
importance of competing effects (i.e. electric field and ion–neutral collision
effects) is discussed. The capability of controlling the charged particle
motions through a combination of directed neutral flow and applied electric
field is demonstrated for high-speed, hypersonic jet flows.

1. Introduction

The ability to predict accurately and thereby understand
the often complex transport of charged particles through a
background neutral gas subject to electro-magnetic forces
is very important to furthering the understanding of many
advanced technological and industrial plasma processes,
including those associated with vapour deposition in material
and semiconductor processing [1, 2], microsystems [3], electric
space propulsion devices [4–8], and ionospheric and space
plasma processes [9, 10]. Transport of ions through rapidly
expanding and/or jet flows is also important to the operation of
mass spectrometers, such as liquid chromatography (LC)/mass
spectrometry (MS) systems used extensively in trace analysis
of biological fluids for drugs, metabolites, and natural
biopolymers [11]. The latter is the particular application
of interest here. LC/MS instruments make use of an
atmospheric pressure ionization technique whereby sample

ions are generated at atmospheric pressure from molecules
that are contained in micro-droplets, and the resulting ions
are then transported from atmospheric pressure conditions into
a high vacuum system for spectroscopic analysis. As might
be expected, the performance of mass spectrometers is highly
dependent on the ion transport from the ion source region to
the mass detectors, and gaining an improved understanding
of ion-source jet flows and related transport phenomena is an
active area of research.

This study is concerned with application of modern
numerical methods to modelling of the transport of free ions
through highly under-expanded jet flows of neutral gases
in the presence of applied electric fields. A five-moment
continuum-based model and parallel multi-block numerical
solution procedure are developed and described for predicting
the ion transport. The five-moment model provides 'one-way'
coupling between the ion and neutral flows by incorporating
the effects of ion–neutral collision processes. It is used in

conjunction with a Navier–Stokes model and flow solver for the neutral gas to examine the key features of the ion motion. The influences of the neutral gas flow, electric field, and flow field geometry on ion mobility are assessed, and numerical results are given relevant to ion flows occurring in the interface region of mass spectrometer systems. The capability of controlling the charged particle motions through a combination of directed neutral flow and applied electric field is demonstrated for high-speed, hypersonic jet flows.

2. Governing equations

2.1. Five-moment ion transport model

The transport of a mixture of a neutral gas and free ions is considered here. This mixture is not formally treated as plasma but rather as a source of positively charged ions for it is assumed that there are no free electrons (plasmas consist of neutral particles, ions, and electrons, and charged particle transport is generally tightly coupled by electric/magnetic applied/induced fields). For the purposes of this study, it is also estimated and assumed that the ion number density is very low compared with the neutral gas, so that the ions have a negligible effect on the neutral particles. Hence, the solution of the ion and neutral gas flows can be decoupled. The neutral gas flow field can be predetermined, and then the prediction of the ion motion can be carried out using this calculated neutral gas solution. A five-moment closure continuum approximation is used herein to model the motion of the ions through the more dense neutral gas [12–15]. This mathematical description is a single-temperature, near-equilibrium model that can take into account the effects of ion–neutral collision processes and applied external electric and magnetic forces. Ion self-collisions (ion–ion collision processes) are neglected in this approximation, and hence the ion fluid stresses and heat flux are assumed to be unimportant.

The governing transport equations of the five-moment model reflect the conservation of mass, momentum, and energy and can be written in non-conservative coordinate-free form as

$$\frac{\partial \rho_i}{\partial t} + \nabla \cdot (\rho_i v_i) = 0, \tag{1}$$

$$\frac{\partial v_i}{\partial t} + (v_i \cdot \nabla) v_i + \frac{1}{\rho_i} \nabla p_i$$
$$= \frac{Q_i}{m_i} E + \frac{Q_i}{m_i} (v_i \times B) + \sum_s \nu_{is} (v_s - v_i), \tag{2}$$

$$\frac{\partial p_i}{\partial t} + (v_i \cdot \nabla) p_i + \gamma_i p_i (\nabla \cdot v_i) = \frac{\delta p_i}{\delta t}, \tag{3}$$

where $\rho_i = m_i n_i$ is the ion mass density, n_i is the ion number density, m_i is the mass of the ion molecules, v_i is the ion velocity, $p_i = \rho_i R_i T_i = n_i k T_i$ is the ion pressure, T_i is the ion temperature, R_i is the ion ideal gas constant, k is the Boltzmann constant, γ_i is the ion specific heat ratio, Q_i is the ion particle charge, and E and B are the external electric and magnetic fields. Ion–neutral collision processes are modelled here using a generalization of the so-called relaxation-time or Bhatnagar, Gross, and Krook (BGK) approximation for the Boltzmann collision integral [12, 14–16]. In this modified relaxation-time approach, the relaxation time is actually not

constant. Instead, the collision cross-section is assumed to be constant and the collision frequency is taken to be dependent on the local macroscopic solution quantities (i.e. number densities and temperatures). The influences of the ion–neutral collisional processes manifest themselves as source terms in the ion momentum and energy equations, equations (2) and (3), respectively. These terms involve a sum over all neutral gas species, s, and depend on the momentum exchange collision frequency, ν_{is}. The energy or pressure source term, $\delta p_i / \delta t$, is given by

$$\frac{\delta p_i}{\delta t} = \sum_s \frac{\rho_i \nu_{is}}{m_i + m_s} \left[2k(T_s - T_i) + \frac{2}{3} m_s |v_s - v_i|^2 \right], \tag{4}$$

where T_s and v_s are the temperature and velocity of neutral species s, and m_s is the mass of the neutral species molecules. The collision frequency, ν_{is}, can be related to the product of the collision cross-section, σ_{is}, neutral species number density, n_s, and relative speed of the colliding particles, g_{is}. By utilizing the approximation that

$$g_{is} = \sqrt{\bar{v}_i^2 + \bar{v}_s^2} = \sqrt{\frac{8kT_i}{\pi m_i} + \frac{8kT_s}{\pi m_s}},$$

the following expression can be obtained and used to prescribe the ion–neutral collision frequency [15]:

$$\nu_{is} = \sigma_{is} n_s g_{is} = \sigma_{is} n_s \sqrt{1 + \frac{m_s T_i}{m_i T_s}} \sqrt{\frac{8kT_s}{\pi m_s}}. \tag{5}$$

The relaxation-time model is only an approximation to the Boltzmann collision integral and ignores the detailed nature of inter-particle interactions. Nevertheless, it retains many of the qualitative features of the true collision integral and is thought to be sufficient for this initial study of ion transport phenomena in mass spectrometer systems.

For a two-dimensional axisymmetric coordinate system, a neutral gas consisting of a single neutral species $s = n$ and negligible magnetic fields ($B = 0$), the conservative form of the five-moment equations governing ion transport can be summarized as follows:

$$\frac{\partial U_i}{\partial t} + \frac{\partial F_i}{\partial z} + \frac{\partial G_i}{\partial r} = S_{ai} + S_{ei} + S_{ci}, \tag{6}$$

where U_i is the conserved variable solution vector given by

$$U_i = [\rho_i, \quad \rho_i u_i, \quad \rho_i v_i, \quad \rho \epsilon_i]^T, \tag{7}$$

z and r are the axial and radial spatial coordinates of the axisymmetric frame, u_i and v_i are the ion axial and radial velocity components, $\epsilon_i = p_i/(\rho_i(\gamma_i - 1)) + |v_i|^2/2$ is the specific total energy, F_i and G_i are the axial- and radial-direction solution flux vectors, given by

$$F_i = \begin{bmatrix} \rho_i u_i \\ \rho_i u_i^2 + p_i \\ \rho_i u_i v_i \\ u_i(\rho_i \epsilon_i + p_i) \end{bmatrix}, \qquad G_i = \begin{bmatrix} \rho_i v_i \\ \rho_i u_i v_i \\ \rho_i v_i^2 + p_i \\ v_i(\rho_i \epsilon_i + p_i) \end{bmatrix}, \tag{8}$$

and S_{ai}, S_{ei}, and S_{ci} are source vectors associated with the axisymmetric coordinate frame, electric fields, and ion–neutral

collision processes, respectively. The latter are given by

$$
S_{ai} = -\frac{1}{r}
\begin{bmatrix}
\rho_i v_i \\
\rho_i u_i v_i \\
\rho_i v_i^2 \\
v_i (\rho_i \epsilon_i + p_i)
\end{bmatrix},
$$

$$
S_{ei} =
\begin{bmatrix}
0 \\
\rho_i \dfrac{Q_i}{m_i} E_z \\
\rho_i \dfrac{Q_i}{m_i} E_r \\
\rho_i \dfrac{Q_i}{m_i} (u_i E_z + v_i E_r)
\end{bmatrix},
\tag{9}
$$

$$
S_{ci} =
\begin{bmatrix}
0 \\
\dfrac{\rho_i m_n \nu_{in}}{m_i + m_n}(u_n - u_i) \\
\dfrac{\rho_i m_n \nu_{in}}{m_i + m_n}(v_n - v_i) \\
\dfrac{1}{\gamma_i - 1}\dfrac{\delta p_i}{\delta t} + \dfrac{\rho_i m_n \nu_{in}}{m_i + m_n}[u_i(u_n - u_i) + v_i(v_n - v_i)]
\end{bmatrix},
\tag{10}
$$

where E_z and E_r are the axial and radial components of the electric field and u_n and v_n are the axial and radial components of the neutral gas velocity. Note the presence of Joule heating terms associated with the applied electric field in the source terms of the energy equation. The equation set of (6) is used here to predict ion particle motion through a high-speed neutral gas.

For low-speed ion flows through a single-species, stationary, neutral gas (neglecting inertial effects), the ion drift velocity can be directly related to the applied electric field. It follows from the ion momentum equation that

$$
v_i = \frac{Q_i}{m_i \nu_{in}} E = \eta_{in} E,
\tag{11}
$$

where $\eta_{in} = Q_i/m_i \nu_{in}$ is the ion mobility. It is readily apparent from this expression that the BGK collision model leads to a linear relationship between drift velocity and electric field.

2.2. Navier–Stokes equations for neutral gas flow

A near-thermal-equilibrium continuum model is also used to describe the neutral gas flows considered in this study. The neutral flow is assumed to be laminar, and the gas is taken to be both calorically and thermally perfect and to obey the ideal gas equation of state, $p_n = \rho_n R_n T_n$, where p_n is the static pressure of the neutral gas, $\rho_n = m_n n_n$ is the neutral gas mass density, n_n is the neutral gas number density, T_n is the neutral gas temperature, and R_n is the gas constant. Due to the low concentration of ion particles relative to the concentration of neutral molecules, ion–neutral inter-particle interactions have an insignificant influence on the motion of the neutral gas. It is therefore appropriate to assume that the neutral gas flow is unaffected by the ion particles. Accordingly, the well known Navier–Stokes equations for a compressible fluid govern the transport of the neutral gas. For a two-dimensional

axisymmetric coordinate system, the conservation form of these equations can be expressed as

$$
\frac{\partial U_n}{\partial t} + \frac{\partial F_n}{\partial z} + \frac{\partial G_n}{\partial r} = \frac{\partial F_{vn}}{\partial z} + \frac{\partial G_{vn}}{\partial r} + S_{an},
\tag{12}
$$

where U_n is the neutral gas conserved variable solution vector given by

$$
U_n = [\rho_n, \quad \rho_n u_n, \quad \rho_n v_n, \quad \rho_n \epsilon_n]^T,
\tag{13}
$$

F_n and G_n are the axial- and radial-direction inviscid flux vectors given by

$$
F_n =
\begin{bmatrix}
\rho_n u_n \\
\rho_n u_n^2 + p_n \\
\rho_n u_n v_n \\
u_n(\rho_n \epsilon_n + p_n)
\end{bmatrix}, \qquad
G_n =
\begin{bmatrix}
\rho_n v_n \\
\rho_n u_n v_n \\
\rho_n v_n^2 + p_n \\
v_n(\rho_n \epsilon_n + p_n)
\end{bmatrix}
\tag{14}
$$

and F_{vn} and G_{vn} are the axial- and radial-direction viscous flux vectors given by

$$
F_{vn} =
\begin{bmatrix}
0 \\
\tau_{n_{zz}} \\
\tau_{n_{rz}} \\
u_n \tau_{n_{zz}} + v_n \tau_{n_{rz}} - q_{n_z}
\end{bmatrix},
$$

$$
G_{vn} =
\begin{bmatrix}
0 \\
\tau_{n_{rz}} \\
\tau_{n_{rr}} \\
u_n \tau_{n_{rz}} + v_n \tau_{n_{zz}} - q_{n_r}
\end{bmatrix}.
\tag{15}
$$

The vector S_{an} contains source and viscous flux terms associated with the axisymmetric geometry and has the form

$$
S_{an} = \frac{1}{r}
\begin{bmatrix}
-\rho_n v_n \\
-\rho_n u_n v_n + \tau_{n_{rz}} \\
-\rho_n v_n^2 + \tau_{n_{rr}} - \tau_{n_{\theta\theta}} \\
-v_n(\rho_n \epsilon_n + p_n) + u_n \tau_{n_{rz}} + v_n \tau_{n_{rr}} - q_{n_r}
\end{bmatrix}.
\tag{16}
$$

The variables u_n and v_n are the axial and radial components of the neutral gas velocity, v_n, respectively, and $\epsilon_n = p_n/(\rho_n(\gamma_n - 1)) + (u_n^2 + v_n^2)/2$ is the specific total energy. The components of the viscous stress tensor, τ_n, are given by

$$
\tau_{n_{ij}} = \mu_n \left(\frac{\partial v_{n_i}}{\partial x_j} + \frac{\partial v_{n_j}}{\partial x_i} - \delta_{ij}\frac{2}{3}\nabla \cdot v_n \right)
\tag{17}
$$

and the axial and radial components of the heat flux vector, q_n, follow from Fourier's law

$$
q_n = -\kappa_n \nabla T_n,
\tag{18}
$$

where μ_n is the dynamic viscosity, κ_n is the thermal conductivity, and γ_n is the specific heat ratio for the neutral gas. Sutherland's law is used to prescribe the viscosity. Equation (12) is used here to model the high-speed flow of the neutral gas. The validity of the preceding equations for describing the high-speed neutral jet flows of interest here has been clearly demonstrated in recent studies by the authors [17, 18].

2.3. Laplace equation for electric potential

This study is concerned with the influence of steady (time-invariant) electric fields on ion transport through a high-speed neutral gas. Assuming that the net charge density in the fluid volume of interest is negligible (i.e. although there is an excess of charge due to the lack of electrons or negative species, space charge effects can be neglected because of the low ion number densities), the stationary applied electric field, E, satisfies Gauss's law, $\nabla \cdot E = 0$. By expressing the electric field in terms of an electric potential, V, such that $E = -\nabla V$, the electric field can be determined by solving a Laplace equation for the electric potential subject to appropriate boundary data. For a two-dimensional axisymmetric coordinate frame, the Laplace equation has the form

$$\nabla^2 V = \frac{\partial^2 V}{\partial z^2} + \frac{\partial^2 V}{\partial r^2} + \frac{1}{r}\frac{\partial V}{\partial r} = 0. \quad (19)$$

The solution of this scalar equation with boundary conditions for the applied voltage provides a description of the steady-state electric field.

3. Numerical solution procedure

3.1. Solution of ion transport equations

A parallel explicit higher order Godunov-type finite-volume scheme is used to solve the five-moment ion transport equations given by equation (6) on multi-block quadrilateral meshes. The proposed scheme determines the ion motion, given a precomputed neutral gas flow field and electric potential. Upwind finite-volume schemes were originally introduced by Godunov [19]. Application and further development of these schemes for the equations of gas dynamics has been well documented in [20–33]. Solution procedures for the neutral gas flow field and electric field are discussed in subsequent subsections.

In this finite-volume approach, the governing equations are integrated over quadrilateral cells of a structured multi-block quadrilateral mesh. The finite-volume formulation applied to cell j is given by

$$\frac{dU_{i_j}}{dt} = -\frac{1}{A_j} \sum_{\text{faces},k} \vec{F}_{i_{jk}} \cdot \vec{n}_{jk} \Delta \ell_{jk} + S_{a_{i_j}} + S_{e_{i_j}} + S_{c_{i_j}}, \quad (20)$$

where $\vec{F}_i = (F_i, G_i)$, A_j is the area of cell j, and $\Delta \ell_{jk}$ and $\vec{n}_{jk}$ are the length of the cell face k and unit vector normal to the cell face or edge, respectively. The numerical fluxes at the faces of each cell are determined from the solution of a Riemann problem. Given the left and right solution states, U_{i_l} and U_{i_r}, at the cell interfaces, the numerical flux is given by

$$\vec{F}_i \cdot \vec{n} = \mathcal{F}_i(U_{i_l}, U_{i_r}, n), \quad (21)$$

where the numerical flux, $\mathcal{F}_i$, is evaluated by solving a Riemann problem in a direction defined by the normal to the face with initial data U_l and U_r. The left and right solution states are determined using the least-squares limited piecewise linear solution reconstruction procedure of Barth [34]. The modified limiter of Venkatakrishnan [35] has also been implemented. In this algorithm, both exact and approximate Riemann solvers can be used to solve the Riemann problem. The Roe linearized Riemann solver [25], the HLLE-type flux function of Linde [36], the HLLC flux function [37], and the exact Riemann solver of Gottlieb and Groth [38] have all been implemented and may be used. For time-accurate calculations, predictor–corrector and fourth order Runge–Kutta time-marching methods are used to integrate the set of ordinary differential equation that result from this spatial discretization of the governing equations. The optimally smoothing multi-stage schemes developed by van Leer *et al* [39] are adopted for steady-state calculations. To cope with numerical stiffness, a semi-implicit treatment is used in the temporal discretization of the source terms associated with axisymmetric geometry, electric field, and ion–neutral collisions.

Following the approach developed by Groth *et al* [40, 41] for computational magnetohydrodynamics, a flexible block-based hierarchical data structure is used to maintain the connectivity of the quadrilateral solution blocks in the multi-block mesh and facilitate automatic solution-directed mesh adaptation according to physics-based refinement criteria. This data structure also lends itself naturally to domain decomposition and thereby enables efficient and scalable implementations of the algorithm on distributed-memory multi-processor architectures. Aspects of the block-based adaptive mesh refinement algorithm and parallel implementation for multi-block quadrilateral mesh are described in the recent work by Groth *et al* [42, 43].

3.2. Solution of Navier–Stokes equations for neutral flow

A commercial computational fluid dynamics flow solver (CFD++, developed by Metacomp Technologies) is used to predict the high-speed expanding neutral gas flows. This flow solver employs an upwind total variation diminishing (TVD) finite-volume spatial discretization scheme in conjunction with a multi-grid accelerated implicit time-marching procedure to solve the compressible axisymmetric form of the Navier–Stokes equations on unstructured triangular meshes [44, 45]. A V-cycle and Gauss–Seidel smoother are employed in the multi-grid convergence acceleration strategy. Clustering of the cells in the computational mesh may be used to help to capture the important features of the complex neutral flows. The commercial solver also has parallel processing capabilities. The parallel implementation of the neutral gas solver has been developed using the MPI library [46] for performing inter-processor communications and the METIS graph partitioning software for performing a domain decomposition of the computational mesh [47]. The neutral flow solution is independent of the ion solution and can be obtained in a separate calculation. Linear interpolation is used to transfer the neutral flow solution from the unstructured triangular mesh used in the solution of the neutral flow equations to the multi-block quadrilateral mesh used by the finite-volume scheme for the ion transport equations.

3.3. Solution of electric potential

An iterative solution procedure is used to solve equation (19) for the electric potential, V, and the electric field is then calculated in terms of the gradient of the potential, $E = -\nabla V$.

Like the neutral flow solution, the electric field is not dependent on the predicted ion solution and can also be determined in a separate independent computation.

4. Numerical results and discussion

The mathematical formulation and solution algorithm outlined above have been used to perform numerical simulations of ion transport for high-speed, under-expanded, axisymmetric jet flows typical of those encountered in atmospheric pressure ionization mass spectrometer systems. The simulations were carried out on a Beowulf-class parallel computing cluster consisting of 26 four-way Hewlett-Packard Alpha ES40 and ES45 SMP servers with 104 processors and 126 Gb of distributed memory. Both free-jet and jet flows with neutral gas skimmers were considered. The results of these computations now follow.

4.1. Axisymmetric free-jet flow

When a high pressure gas is exhausted through an orifice into a stagnant low-pressure chamber, the gas rapidly expands and results in the formation of an under-expanded free jet [48–50]. A schematic diagram of the under-expanded free jet is shown in figure 1. At the orifice, the flow is for the most part supersonic. The upstream high-pressure gas is therefore unaffected by the downstream flow conditions, and the jet structure must adjust to match the back pressure in the low-pressure chamber. The resulting free-jet flow is quite complex and characterized by thin non-isentropic regions (shocks) with large gradients in the properties of the gas. Key features of an under-expanded free jet include the (i) barrel (intercepting) shock; (ii) jet boundary; (iii) triple point; (iv) Mach disc; and (v) reflected shock.

The numerical solution of an under-expanded free-jet flow of a neutral gas consisting of diatomic nitrogen obtained using a 41 000-cell unstructured triangular grid is shown in figure 2. For this case, the orifice diameter, $d_\circ$, is 0.75 mm, the upstream pressure, $p_\circ$, and temperature, $T_\circ$, are 760 Torr and 288 K,
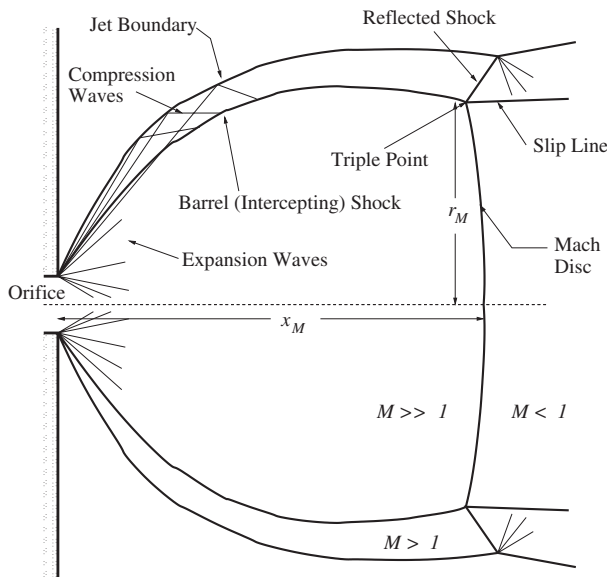
and the downstream pressure, p_b, is 0.5 Torr. The figure depicts the predicted neutral flow streamlines and computed distributions of Mach number $M_n = |v|_n/a_n$ and entropy change $\Delta s_n = (R_n/(\gamma_n - 1)) \ln((p_n/p_\circ)/(\rho_n/\rho_\circ)_n^\gamma)$, where a_n is the sound speed of the neutral gas. The black coloured streamlines are associated with neutral gas flow that passes through the Mach disc, whereas the white coloured stream traces are associated with flow that passes through a region above the triple point via the intercepting shock. The purple coloured streamline marks the boundary between flow passing through the Mach disc and flow passing above the triple point. The green coloured stream traces reflect the viscous entrainment of the low-pressure reservoir gas into the free-jet flow that occurs in the mixing layer at the jet boundary. The flow is highly expanded downstream of the orifice. The pressure decreases by five orders in magnitude in the free jet and then increases abruptly again, following the Mach disc to match the background pressure. The density and temperature also decrease and the flow speed increases monotonically. The Mach number exceeds 12 in the core region of the jet. The intercepting shock, jet boundary, triple point, Mach disc, and reflected shock are all quite evident in the predicted entropy and Mach number distributions and appear to be well resolved.

Detailed results of comparisons between measured and predicted neutral gas pressures for this free-jet flow are described in other recent works of Jugroot *et al* [17, 18]. Overall, the agreement between the experimental data and numerical results was found to be very good. In particular, the boundaries and extent of the free jet were found to be well predicted by the neutral gas flow solver. This provides strong support for the validity and reliability of the neutral gas calculations used in the ion transport modelling herein.
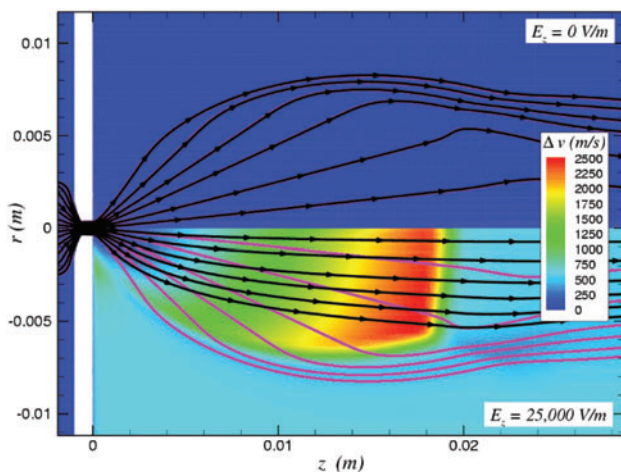
As a first step to understanding ion transport processes in high-speed jets, the transport of ion particles through the preceding under-expanded free-jet flow was studied. In particular, the transport of singly charged ion particles (ion B in table 1) was considered with a molecular weight of 228 amu (dodecyltrimethyl ammonium, $C_{15}H_{34}N$), specific heat ratio

Figure 1. Schematic diagram of free-jet flow shock structure.
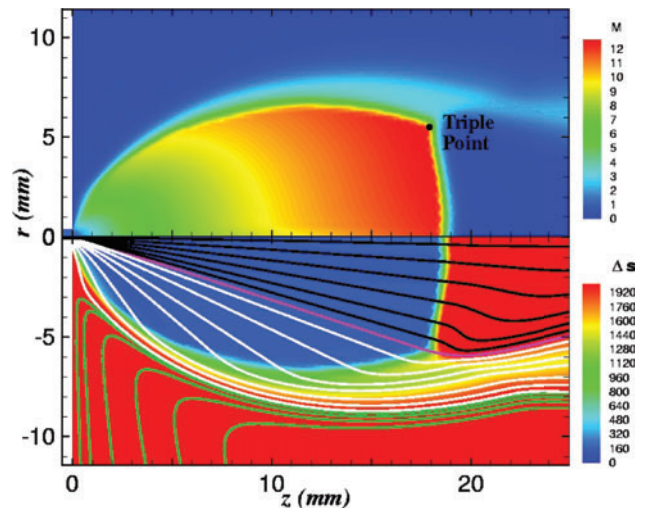
Figure 2. Computed flow streamlines and distributions of Mach number, M_n, and entropy change, Δs_n, for axisymmetric under-expanded free-jet flow with an orifice diameter of $d_\circ = 0.75$ mm and pressure ratio $p_\circ/p_b = 1520$.
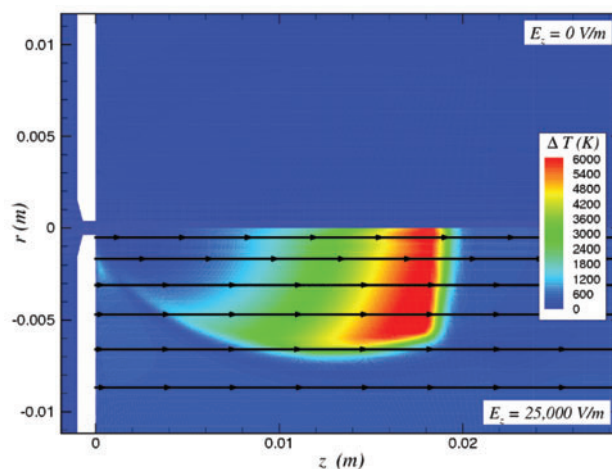
Table 1. Physical properties of ion particles.

Ion	A	B	C	D
Mass (amu)	105	228	609	16 951
Charge	+1	+1	+1	+9
σ_i (10^{-20} m^2)	105	150	280	2560
γ_i	1.2	1.1	1.1	1.05

Figure 3. Computed ion particle (black) and neutral gas (purple) streamlines and distributions of the difference between the ion and neutral gas velocities $\Delta v = |v_i - v_n|$, for under-expanded free-jet flow with an orifice diameter of $d_\circ = 0.75$ mm and pressure ratio $p_\circ/p_b = 1520$. Results are shown for ion B and two values of the axial component of the electric field: $E_z = 0$ V m^{-1} (upper-half plane) and $E_z = 25\,000$ V m^{-1} (lower-half plane).

Figure 4. Computed field lines of the applied electric potential and distributions of the difference between the ion and neutral gas temperatures, $\Delta T = T_i - T_n$, for an under-expanded free-jet flow with an orifice diameter of $d_\circ = 0.75$ mm and pressure ratio $p_\circ/p_b = 1520$. Results are shown for ion B and two values of the axial component of the electric field: $E_z = 0$ V m^{-1} (upper-half plane) and $E_z = 25\,000$ V m^{-1} (lower-half plane).
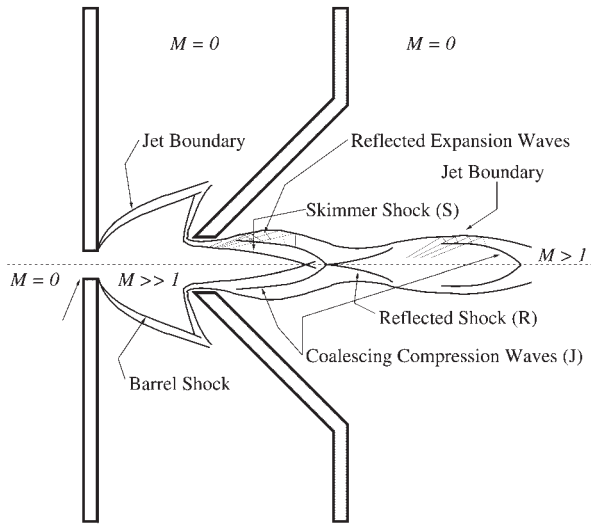
5. Axisymmetric skimmer flows

Having explored features of ion transport for free-jet flows, jet flows with neutral gas skimmers are now considered. Gas skimmers, as shown in figures 5 and 6, are introduced in the interface region of mass spectrometer systems to reduce the flux of neutral gas to the ion optics and to focus ions that are being transported by the neutral flow. Ion transport is studied herein for supersonic jets emanating from orifices of diameters $d_\circ = 0.75$ and 0.25 mm with an axisymmetric conical-shaped skimmer having a skimmer orifice diameter of $d_s = 2.5$ mm and a cone angle of $\alpha_s = 60°$. The transport of ion particles is considered for several different ions with varying mass-to-charge ratios, and the influences of the applied electric field and neutral particles collisions are assessed. Table 1 provides a summary of the ions considered. The four positively charged ion particles given in the table correspond to the following: A (a generic low mass-to-charge ion); B (dodecyltrimethyl ammonium, C$_{15}$H$_{34}$N); C (a reserpine protonated molecule); and D (myoglobin—a protein).

For these cases, differential pumping is used such that the back pressure between the orifice and the skimmer, p_b, is maintained at 1 Torr and the back pressure downstream of the skimmer, p_s, is lower and has a value of 0.005 Torr. In addition, the applied electric voltage is relatively strong: 80 V is applied to the orifice while the gas skimmer is grounded, yielding values in excess of $E = 70\,000$ V m^{-1} near the tip of the skimmer. Figure 6 shows the distribution of the potential in the skimmer region for an orifice diameter of $d_\circ = 0.25$ mm. The electric field for $d_\circ = 0.75$ mm is very similar and not shown. The diverging field lines shown in the figure confirm that the electric field is highly non-uniform.

The overall structure of the neutral flow with a gas skimmer is very different from that of the free jet. The presence of the skimmer disrupts and prevents the jet from fully expanding. As a consequence, a Mach disc does not form. Unlike the free-jet case, the neutral gas remains highly

$\gamma_i = 1.2$, and a constant cross-section of $\sigma_{in} = 1.50 \times 10^{-18}$ m^2 for collisions with neutral nitrogen particles. The ions upstream of the orifice were assumed to be in equilibrium with the neutral gas, and the upstream number density of the ions was taken to be $n_i = 10^{14}$ m^{-3}. Constant axial electric fields of varying magnitude were applied, and numerical solutions were obtained using the parallel finite-volume method described earlier. A total of 13 solutions blocks and 24 500 quadrilateral computational cells were used in the computations.

Figures 3 and 4 show the numerical results for the ion transport in the case of an under-expanded free jet. The computed ion and neutral gas streamlines, electric field lines, and distributions of the differences between the ion and neutral gas velocities and temperatures are shown. In the absence of an electric field ($E_z = 0$ V m^{-1}), it can be seen that the ion–neutral collision frequency is sufficient to maintain equilibrium conditions between ions and neutral particles such that $v_i = v_n$ and $T_i = T_n$. When the electric field becomes sufficiently strong ($E_z = 25\,000$ V m^{-1}), the electric forces then dominate the ion motion in the high-speed regions of the free-jet flow downstream of the orifice with low neutral gas density. The ion particles undergo a rapid acceleration by the electric field and attain velocities in excess of 2.5 km s^{-1} above those of the neutrals. At the same time the Joule heating and drag forces due to collisions with the neutrals produce significant heating of the ions. Temperatures in excess of 7000 K in this particular example are predicted.

Figure 5. Schematic diagram of skimmer jet-flow shock structure showing the skimmer shock (S); the coalescing reflected compression waves from the jet boundary (J); the reflected shock (R); and the succession of expansion/re-compression cells.
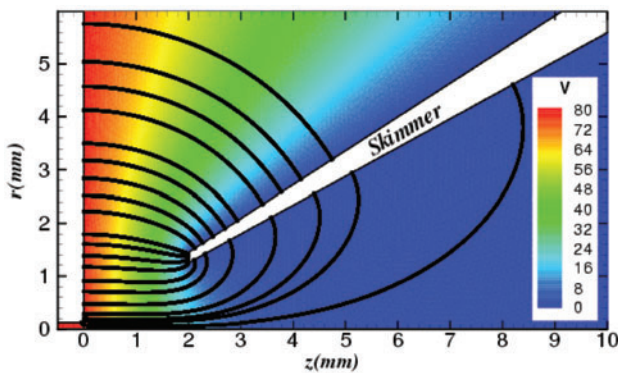

Figure 6. Computed applied electric potential, V, and field lines for under-expanded skimmer jet flow with an orifice diameter of $d_\circ = 0.25$ mm. The potential on the orifice is 80 V, and the skimmer is grounded.

supersonic in the core of the jet far downstream of the orifice and skimmer. The skimmer not only confines the jet expansion process but also acts to divide the neutral flow, diverting a significant portion of the neutral particles. The flow structure of the neutral gas in the presence of skimmers is discussed in detail in the recent work of Jugroot *et al* [17, 18]. Figure 5 provides a schematic diagram of the skimmer flow and shock structure, illustrating the skimmer shock and succession of expansion/re-compression cells occurring downstream of the skimmer orifice.

Figure 7 shows the numerical simulation of ion transport for ion B (mass-to-charge ratio of 228) for the larger diameter jet (orifice diameter $d_\circ = 0.75$ mm). The computed distribution of the current density, $J = |J| = Q_i n_i |v_i|$, for ion B indicates that most of the ions go through the skimmer as a result of combined effects of entrainment by the neutral supersonic gas and the applied electric field. Figure 8 shows additional predictions of ion transport for the smaller diameter jet with an orifice diameter of 0.25 mm. The computed ion and neutral gas streamlines and distribution of ion velocity
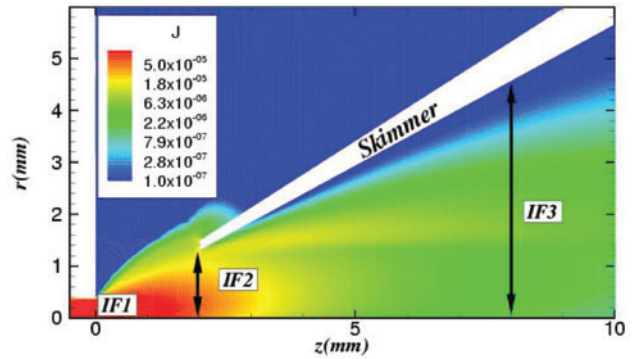

Figure 7. Computed distributions of the current density, $J = |J| = Q_i n_i |v_i|$ (A m^{-2}), for ion B in an under-expanded skimmer jet flow with orifice diameter of $d_\circ = 0.75$ mm. Stations IF1, IF2, and IF3 refer to the axial positions where the ion flux tabulated in table 2 has been evaluated.
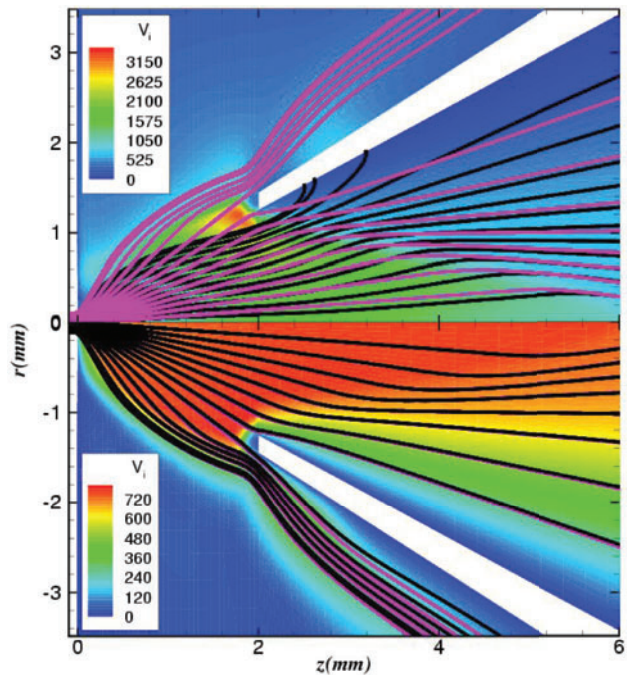
Figure 8. Computed ion particle (black) and neutral gas (purple) streamlines and distributions of the ion velocity (m s^{-1}) for under-expanded skimmer jet flow with an orifice diameter of $d_\circ = 0.25$ mm. Results are shown for two ions: the upper-half plane corresponds to ion B and the lower-half plane to ion D.

are shown for both ions B and D. Ion D has a much larger mass-to-charge ratio of 1884.

For ion B, it can be observed that the neutral gas is partially diverted by the skimmer, whereas all ion streamlines pass through the skimmer. At the exit of the orifice and in its close vicinity, the ions follow the neutral gas, but as they approach the skimmer region, the ion trajectories clearly deviate from those of the neutrals due to the strong imposed electric field. The applied electric field is non-uniform as a result of the point-to-plane type configuration and dominates the ion motion in the high-speed regions of the jet flow downstream of the orifice. In this region, the neutral gas becomes more and more dilute and the relative importance of the electric field on ion motion grows as its magnitude increases
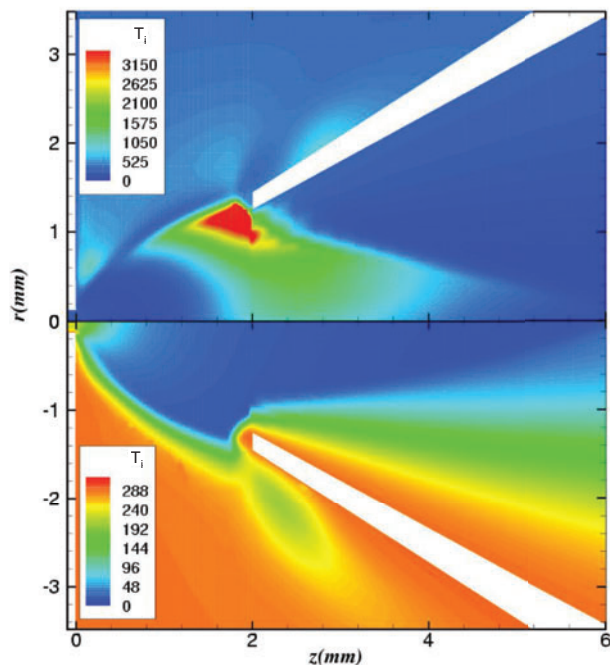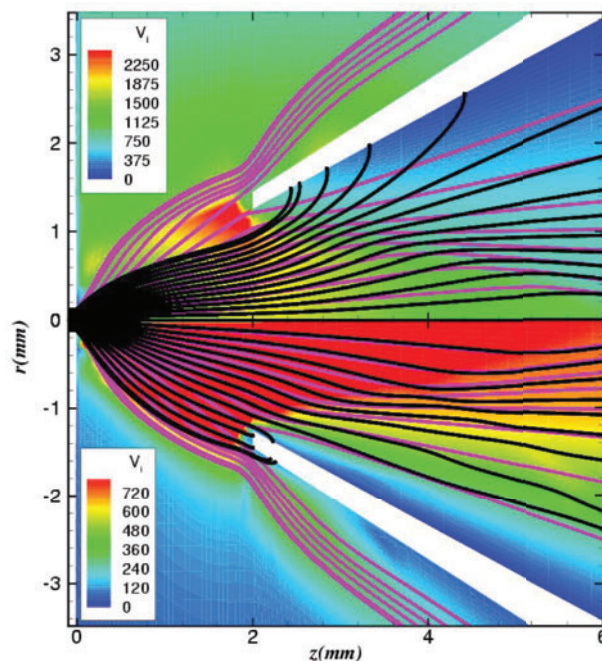
Figure 9. Computed distribution of ion temperature (K) for under-expanded skimmer jet flow with an orifice diameter of $d_\circ = 0.25$ mm. Results are shown for two ions: the upper-half plane corresponds to ion B and the lower-half plane to ion D.

Figure 10. Computed ion particle (black) and neutral gas (purple) streamlines and distributions of the ion velocity (m s^{-1}) for under-expanded skimmer jet flow with an orifice diameter of $d_\circ = 0.25$ mm. Results are shown for two ions: the upper-half plane corresponds to ion A and the lower-half plane to ion C.

rapidly. The particles of ion B are strongly accelerated by the electric field and attain much higher velocities than the neutrals as depicted in figure 8. Joule heating and drag forces due to collisions with the neutrals produce heating of the ions near the tip of the skimmer, and temperatures exceeding 5000 K are observed as shown in figure 9. The high temperatures predicted for ion B would probably initiate ion breakdown at the tip of the skimmer. It should be further noted that the neutral-to-ion pressure ratio in the core of the jet flow is about 10^{10}, hence justifying the one-way coupling adopted herein for predicting the coupled ion/neutral transport.

The predicted ion motions for the other ions of varying mass-to-charge ratios (ions A, C, and D) are in general much the same as that for ion B in the vicinity just downstream of the jet orifice, as illustrated in figures 8 and 10. However, as the electric field grows in strength and the neutral gas becomes more dilute near the skimmer tip, the differences in the transport of the ions of varying mass-to-charge ratios become apparent. The ions exhibit a clear tendency to follow the diverging electric field lines. The extent of this phenomenon is directly dependent on the mass of the ion and its charge. The ion with the lowest mass-to-charge ratio, ion A, is most influenced by the electric field and follows closely the field lines, whereas ion D is almost unaffected by the electric field due to its high mass-to-charge ratio, as seen in figures 8 and 10.

The tendency of the lower mass ions to follow the electric field has a direct impact on the ion currents or mass flux through the skimmer. The computed ion flux ratios for ions A, B, C, and D at the skimmer (station IF2) and 6 mm downstream of the skimmer (station IF3), normalized to the reference value determined at the exit of the jet orifice (station IF1), are summarized in table 2. The electric field causes a greater

Table 2. Ion flux through skimmer (IF2) and downstream of the skimmer (IF3) as a percentage of the reference value through the orifice (IF1) for an orifice diameter of $d_\circ = 0.25$ mm. Refer to figure 7 for the locations of stations IF1, IF2, and IF3.

Ion	A	B	C	D
IF2 (%)	94	86	53	39
IF3 (%)	59	68	36	38

number of the lower mass ions to pass through the skimmer (94% of ion A particles pass through the skimmer orifice as compared with 39% for ion D). Interestingly enough, the lower mass ions are also more readily induced by the diverging electric field to impact the skimmer downstream of the skimmer orifice, thereby reducing the effective ion mass flux through the skimmer (only 59% of ion A particles pass through the skimmer at station IF3, whereas virtually all ion D particles that pass through the skimmer orifice also pass through the skimmer at station IF3).

Beyond the skimmer tip region, where the electric field gradually diminishes, all ions again tend to follow the neutral gas trajectory, characterized by a flow deflection produced by the skimmer leading edge conical-shaped shock that subsequently reflects from the axis of symmetry [17, 18]. In the absence of an applied electric field ($E = |\boldsymbol{E}| = 0\,\mathrm{V\,m^{-1}}$), the ion–neutral collision frequency is sufficient to maintain equilibrium conditions between ions and neutral particles such that $v_i = v_n$ and $T_i = T_n$. In general, the differences between the ion and neutral trajectories are negligible for all the ions considered here when the electric field is absent.

A better understanding of the ion transport can be obtained by considering the relative effects of ion–neutral collision processes on the ion motion as compared with the effects of
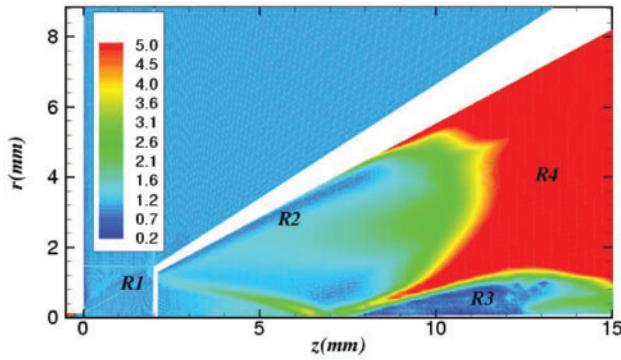
Figure 11. Computed distribution of the ratio of the one-norm of the momentum source terms due to ion–neutral collisions to the one-norm of the moment sources terms for the electric field as given in equations (9) and (10), for ion A in an under-expanded skimmer jet flow with an orifice diameter of $d_\circ = 0.25$ mm.

the applied electric field. The ratio of the one-norm of the momentum source terms associated with ion–neutral collisions (both axial and radial momentum components) to the one-norm of the momentum source terms due to the electric field can be evaluated. These source terms are given in equations (9) and (10). The ratio of the norms of the momentum source terms provides an indication of the relative importance of the neutral drag due to collisional processes as compared with the ion acceleration produced by the imposed electric field. Computed values of this ratio are depicted in figure 11 for ion A in an under-expanded jet flow with an orifice diameter of $d_\circ = 0.25$ mm. It is interesting to observe that different regions of the simulated flow field are either collisionally regulated or regulated by the electric field, while still other regions of the flow exhibit an equilibrium between these two competing effects. Near the tip of the skimmer (region R1), the electric field is only slightly dominant, in spite of the fact that the electric field is very strong in this region. This is because the neutral gas density rises sharply in the vicinity of the skimmer bow shock. However, in region R2, it is clear that the electric field exerts relatively more influence on the ions than the neutrals. The electric field appears again to be more dominant in region R3, but this is not due to a strong applied electric field but rather a result of the neutral density increasing following the reflection of the skimmer bow shock from the axis of symmetry. The increased neutral gas density in this region leads to near-equilibrium conditions between the ion and neutral gas velocities. Further downstream in region R4, collisional effects exert more influence on the ion motions as the electric field becomes negligible.

6. Conclusions

The transport of free ions through highly under-expanded jet flows of neutral gases and in the presence of applied electric fields has been investigated using continuum-based numerical simulations. A five-moment mathematical model and parallel multi-block numerical solution procedure has been developed and described for predicting the ion transport. The model incorporates the effects of ion–neutral collision processes and is used in conjunction with a Navier–Stokes flow solver for

the neutral gas to examine the key features of the ion motion. The influences of the neutral gas flow, electric field, and flow field geometry on ion mobility have been demonstrated for typical flow conditions and geometries found in the interface region of mass spectrometer systems. The combined effect of the applied electric field and neutral collision processes with the diluted background gas results in a tendency of ion focusing towards the axis, with the overall efficiency of the focusing being governed by the mass-to-charge ratio. Future work will involve extending the modelling to three-dimensional flow geometries and investigating the application of high-order moment models to describe non-equilibrium ion transport phenomena.

References

[1] Meyyappan M (ed) 1995 *Computational Modeling in Semiconductor Processing* (Boston: Artech House)
[2] Lieberman M A and Lichtenberg A J 1994 *Principles of Plasma Discharges and Materials Processing* (New York: Wiley)
[3] Jugroot M, Bayle P, Yousfi M and Eichwald O 1999 *J. Phys. D: Appl. Phys.* **32** 106
[4] Brophy J R and Noca M 1998 *J. Propulsion Power* **14** 700
[5] Martinez-Sanchez M and Pollard J E 1998 *J. Propulsion Power* **14** 688
[6] Jugroot M and Harvey J K 2001 *Aeronaut. J.* **105** 613
[7] Jugroot M and Harvey J K 2001 IEPC Paper 01-100 *27th International Electric Propulsion Conf. (Pasadena, CA)*
[8] Krülle G, Auweter-Kurtz M and Sasoh A 1998 *J. Propulsion Power* **14** 754
[9] Schunk R W and Nagy A F 2000 *Ionospheres: Physics, Plasma Physics and Chemistry* (New York: Cambridge University Press)
[10] Cravens T E 1997 *Physics of Solar System Plasmas* (New York: Cambridge University Press)
[11] Thomas R 2001 *Spectroscopy* **16** 28
[12] Burgers J M 1969 *Flow Equations for Composite Gases* (New York: Academic)
[13] Barakat A R and Schunk R W 1982 *Plasma Phys.* **24** 389
[14] Gombosi T I and Rasmussen C E 1991 *J. Geophys. Res.* **96** 7759
[15] Gombosi T I 1994 *Gaskinetic Theory* (Cambridge: Cambridge University Press)
[16] Bhatnagar P L, Gross E P and Krook M 1954 *Phys. Rev.* **94** 511
[17] Jugroot M, Groth C P T, Thomson B, Baranov V and Collings B A 2002 *Proc. 10th Annual Conf. CFD Society of Canada (Windsor, Ontario)*
[18] Jugroot M, Groth C P T, Thomson B, Baranov V and Collings B A 2003 *J. Phys. D: Appl. Phys.* submitted
[19] Godunov S K 1959 *Mat. Sb.* **47** 271
[20] van Leer B 1973 *Lecture Notes in Physics* vol 18 (New York: Springer) p 163
[21] van Leer B 1974 *J. Comput. Phys.* **14** 361
[22] van Leer B 1977 *J. Comput. Phys.* **23** 263

[23] van Leer B 1977 *J. Comput. Phys.* **23** 276
[24] van Leer B 1979 *J. Comput. Phys.* **32** 101
[25] Roe P L 1981 *J. Comput. Phys.* **43** 357
[26] van Leer B 1982 *Lecture Notes in Physics* vol 170 (New York: Springer) p 507
[27] Colella P and Woodward P R 1984 *J. Comput. Phys.* **54** 174
[28] Harten A 1983 *J. Comput. Phys.* **49** 357
[29] Harten A 1984 *SIAM J. Numer. Anal.* **21** 1
[30] Osher S and Chakravarthy S R 1984 *SIAM J. Numer. Anal.* **21** 955
[31] Roe P L 1984 Generalized formulation of TVD Lax-Wendroff schemes *Report* 84-53 ICASE
[32] Yee H C 1987 *J. Comput. Phys.* **68** 151
[33] Harten A, Enquist B, Osher S and Chakravarthy S R 1987 *J. Comput. Phys.* **71** 231
[34] Barth T J 1993 AIAA Paper 93-0668 *31st AIAA Aerospace Sciences Meeting and Exhibit (Reno, NV)*
[35] Venkatakrishnan V 1993 AIAA Paper 93-0880 *31st AIAA Aerospace Sciences Meeting and Exhibit (Reno, NV)*
[36] Linde T J 1998 A three-dimensional adaptive multifluid MHD model of the heliosphere *PhD Thesis* University of Michigan
[37] Toro E F, Spruce M and Speares W 1994 *Shock Waves* **4** 25
[38] Gottlieb J J and Groth C P T 1988 *J. Comput. Phys.* **78** 437
[39] van Leer B, Tai C H and Powell K G 1989 AIAA Paper 89-1933-CP *9th AIAA Computational Fluid Dynamics Conf. (Buffalo, New York)*
[40] Groth C P T, Zeeuw D L D, Powell K G, Gombosi T I and Stout Q F 1999 AIAA Paper 99-3273 *14th AIAA Computational Fluid Dynamics Conf. (Norfolk, VA)*
[41] Groth C P T, De Zeeuw D L, Gombosi T I and Powell K G 2000 *J. Geophys. Res.* **105** 25,053
[42] Groth C P T, Tsang K and Li E 2003 *Proc. 11th Annual Conf. CFD Society of Canada (Vancouver, BC)*
[43] Sachdev J S, Groth C P T and Gottlieb J J 2003 *Int. J. Comput. Fluid Dyn.* submitted
[44] Peroomian O, Chakravarthy S and Goldberg U C 1997 AIAA Paper 97-0724 *35th AIAA Aerospace Sciences Meeting and Exhibit (Reno, NV)*
[45] Peroomian O, Chakravarthy S and Goldberg U C 1998 AIAA Paper 98-0116 *36th AIAA Aerospace Sciences Meeting and Exhibit (Reno, NV)*
[46] Gropp W, Lusk E and Skjellum A 1999 *Using MPI* (Cambridge, MA: MIT Press)
[47] Karypis G and Kumar V 1998 *J. Parallel Dist. Comput.* **48** 96
[48] Ashkenas H and Sherman F S 1966 *Rarefied Gas Dynamics* (New York: Academic) p 84
[49] Crist S, Sherman P M and Glass D R 1966 *AIAA J.* **4** 68
[50] Abbet M 1971 *AIAA J.* **9** 512